Journal of Biomedical Optics

BiomedicalOptics.SPIEDigitalLibrary.org

Methods and algorithms for optical coherence tomography-based angiography: a review and comparison

Anqi Zhang
Qinqin Zhang
Chieh-Li Chen
Ruikang K. Wang

SPIE.

Journal of Biomedical Optics 20(10), 100901 (October 2015)

REVIEW

Methods and algorithms for optical coherence tomography-based angiography: a review and comparison

Anqi Zhang, Qinqin Zhang, Chieh-Li Chen, and Ruikang K. Wang*
University of Washington, Department of Bioengineering, Seattle, Washington 98195, United States

Abstract. Optical coherence tomography (OCT)-based angiography is increasingly becoming a clinically useful and important imaging technique due to its ability to provide volumetric microvascular networks innervating tissue beds *in vivo* without a need for exogenous contrast agent. Numerous OCT angiography algorithms have recently been proposed for the purpose of contrasting microvascular networks. A general literature review is provided on the recent progress of OCT angiography methods and algorithms. The basic physics and mathematics behind each method together with its contrast mechanism are described. Potential directions for future technical development of OCT based angiography is then briefly discussed. Finally, by the use of clinical data captured from normal and pathological subjects, the imaging performance of vascular networks delivered by the most recently reported algorithms is evaluated and compared, including optical microangiography, speckle variance, phase variance, split-spectrum amplitude decorrelation angiography, and correlation mapping. It is found that the method that utilizes complex OCT signal to contrast retinal blood flow delivers the best performance among all the algorithms in terms of image contrast and vessel connectivity. The purpose of this review is to help readers understand and select appropriate OCT angiography algorithm for use in specific applications. [DOI: 10.1117/1.JBO.20.10.100901]

Keywords: optical coherence tomography; optical coherence tomography-based angiography; optical microangiography; retinal imaging.

Paper 150393VR received Jun. 10, 2015; accepted for publication Sep. 28, 2015; published online Oct. 16, 2015.

1 Introduction

Optical coherence tomography (OCT) has become one of the most powerful imaging modalities over the last two decades[1–6] due to its useful capability of generating depth resolved cross-sectional images of biological tissue with excellent sectioning ability (1- to 10-μm resolution). Its capability of high-resolution imaging is achieved through light temporal coherence gating together with confocal detection using optical fiber-based system. OCT has already become a clinical diagnostic tool for structural (anatomical) imaging as well as therapeutic monitoring in ophthalmology for many years.[3] In addition to its usage in ophthalmology, it has drawn an increased attention in other medical disciplines, for example, dermatology,[7,8] gastroenterology,[9] cardiology,[10] and neurology.[11] Paralleled with the rapid development of light source and detection techniques, OCT has been explored and extended drastically not only for structural imaging but also for functional imaging, such as optical microangiography (OMAG).

The OCT-based angiography is now lifting the OCT applications to a new height since it can noninvasively provide functional information about the dynamics of blood vessel networks, which is otherwise difficult to obtain by the use of the traditional OCT for which the contrast mechanism is based on light backscattering. This functional information is likely to provide insights that can improve our understanding of the pathophysiology of various disease conditions that have vascular involvement. In ophthalmology, for example, diabetic retinopathy (DR) often involves retinal capillary complications and sometimes neovascularization;[12] glaucoma is associated visual field loss that is highly correlated with reduction in retinal blood flow;[13] and neovascular age-related macular degeneration (AMD) is characterized by the presence of choroidal neovascularization, accounting for the majority of AMD-related vision loss.[14] Without a need for exogenous contrasting agent, the recent OCT-based angiography has indicated its great advantage over the current clinical standard imaging techniques for visualizing functional retinal blood vessels, such as fluorescein angiography (FA) and indocyanine green angiography.[15]

To understand the current various OCT angiography methods, we first revisit the OCT signals in Fourier-domain OCT (FD-OCT), which can be approximated by assuming a light source with Gaussian shaped power spectral density:[16–18]

$$\Im^{-1}\{I_{\mathrm{OCT}}(k)\}(z) = 2r_R I_0 \sum_{j=1}^{n} r_S(z_j)\gamma[2(z-z_j)] \times \exp[-i2k_0(z-z_j)], \quad (1)$$

$$\Im^{-1}\{I_{\mathrm{OCT}}(k)\}(z) = A(z)\exp[-i\Phi(z)], \quad (2)$$

where $\Im^{-1}\{F(\xi)\}(x)$ denotes inverse Fourier transform of function $F(\xi)$ with variable x; $I_{\mathrm{OCT}}(k)$ is the raw spectrum detected in k space; r_R is the reference arm field reflectance; the summation $\sum_{j=1}^{n}$ denotes n simultaneously detected backscattering events; $r_S(z_j)$ is the sample arm field reflectance for jth backscattered event that was detected from depth z_j; $\gamma[2(z-z_j)]$ is the normalized temporal autocorrelation function, which denotes the coherence gating ability of the light source and

*Address all correspondence to: Ruikang K. Wang, E-mail: wangrk@uw.edu

provides the axial resolution of OCT; $\exp[-i2k_0(z-z_j)]$ is the phase term associated with the jth backscattered event originated from the depth z_j. The right hand side of Eq. (1) is the depth z encoded complex OCT function after taking the inverse Fourier transform of the detected k spectrum, and its magnitude denotes the structural OCT image. Note that for brevity, the SD-OCT configuration, in which a line array detector is used for the detection of spectral interferograms, is considered for the most parts of discussions below. However, there is no reason to believe that these discussions are not applicable to swept-source (SS)-OCT configuration.

The OCT signal after Fourier transformation contains both magnitude and phase information, as indicated in Eq. (2), which have both been explored, either individually or combined, to develop angiographic methods for the purpose of contrasting the blood flow within living tissue. Therefore, the various angiographic approaches can be roughly categorized but not limited into three groups: (1) angiography based on both the magnitude and phase of OCT signal, i.e., complex signal; (2) angiography based on the magnitude of OCT signal, and (3) angiography based on the phase of OCT signal.

In this review, the development of OCT angiography in each category is described, and the principle of each algorithm is briefly introduced. Then, potential directions for future development of OCT angiography are discussed. At last, we compare and discuss the performance of several recent angiography approaches that were reported with clinical applications, including OMAG, speckle variance, phase variance, split-spectrum amplitude decorrelation angiography (SSADA), and correlation mapping. These methods are evaluated using two sets of clinical data acquired from one normal and one pathological subject, respectively. It should be noted that this review is intended to give readers a general survey of the principles of existing OCT angiography approaches, which provide *en-face* blood vessel network visualization with an emphasis on those that were recently reported in the literature.

2 Principle and Development of Optical Coherence Tomography-Based Angiography

2.1 *Angiography Based on the Complex Optical Coherence Tomography Signal*

The first demonstration of OCT angiography within this category, to our knowledge, was proposed by Wang et al., in 2007, in which a novel processing method was presented to explore the changes in signal frequency embedded in raw spectrum in k-space.[19] There are a number of factors that may cause a change in the OCT signal frequency relative to the signal due to static tissue background. These factors include, for example, the Doppler effect that induces optical frequency shift and the change in backscattering due to the particles that are moving in and out of the OCT-probe volume during imaging. The changes in signal frequency cause the changes in phase of the OCT signal. This new optical angiography approach was initially termed as OAG, and later renamed as OMAG. In order to avoid confusion with ultrahigh sensitive OMAG that will be discussed in the next section, we will use the abbreviation OAG in this section.

In theory, as indicated in Eq. (1) the phase of the OCT signal at the depth z is $2k_0(z-z_j)$ if single moving particle at depth z_j is considered. This consideration is sometimes useful to better understand this algorithm due to its simplicity. In this case, the phase change, $\Delta\Phi$, between two A-lines within a time interval t originates from the depth change of the moving particle as δz so that

$$\Delta\Phi = 2k_0\delta z. \tag{3}$$

Assuming the moving particle is with a velocity v_j, such that $\delta z = v_j t$, Eq. (3) can be rewritten as

$$\Delta\Phi = 2k_0 v_j t. \tag{4}$$

Considering the equivalent Doppler shift due to the movement of particle as ω_j, the phase difference induced by this Doppler shift can be expressed as

$$\Delta\Phi = \omega_j t. \tag{5}$$

Comparing Eqs. (4) and (5) leads to

$$v_j = \frac{\omega_j}{2k_0}. \tag{6}$$

Equation (6) indicates that the velocity of moving particle can also be acquired from the Doppler shift ω_j. The raw data in k-space for each B-scan is a two-dimensional (2-D) array with vertical axis being the k component (i.e., k axis) and the longitudinal axis being the lateral scanning position x. The latter variable, x, can also be regarded in time t as t axis. The nature of light temporal coherence determines that the interference fringe comes from the coherent addition of the electric fields originating from both the sample and the reference arms. For each k component in the k-space, the inclusion of moving particle with ω_j at the time t leads to a change in phase $\Delta\Phi$, resulting in a change in fringe signal in the k-t space. The change in fringe frequency for each particular k component would correspond to a change in the frequency of phase $\Delta\Phi$, determined by Doppler shift ω_j. Thus, ω_j in the k-ω space can be determined by taking Fourier transformation along t axis in the k-t space. A typical k-ω space by using a piezoelectric mirror in the sample arm with velocity v_j is illustrated in Fig. 1(a).[20] However, biological tissue is optically heterogeneous, which would induce a frequency broadening around the DC components, as indicated by Wang et al.,[21] providing insights into the influence of optically heterogeneous properties of biological tissue upon angiographic results. Considering multiple flow velocities presented within a sample, a typical distribution of Doppler shifts at one particular k component is indicated in Fig. 1(b).[22] The frequency broadening due to the static tissue background is illustrated in gray around zero frequency while the Doppler shifts due to the moving particles are in red. For clarity, we term such processing scheme as Doppler domain processing method.

A modulation frequency f_m was introduced into the OCT signals by using a piezoelectric mirror in the reference arm[19] or offsetting the galvoscanner,[23,24] which shifted all the Doppler frequencies, as shown in Fig. 1(b) by f_m. This fact leads to that most Doppler frequencies would have positive values. Hence, taking the Hilbert transform of the 2-D k-t space data along the time t axis followed by the Fourier transform along the k axis leads to a separation of flow with negative ω values appearing in negative depth plane from the rest of pixels appearing in positive depth plane. With this treatment, researchers

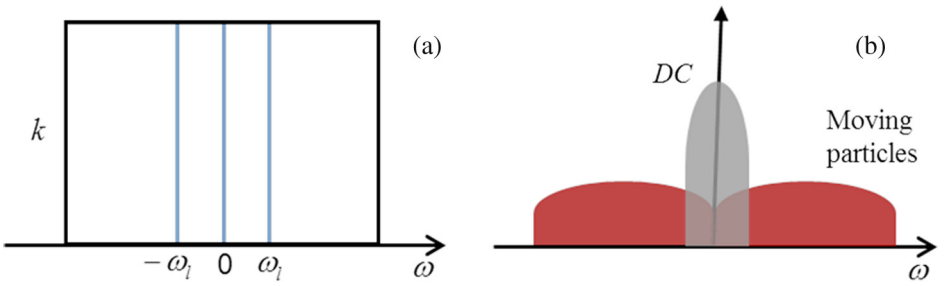

Fig. 1 The k-ω space of optical coherence tomography (OCT) data. (a) The Doppler shifts due the movement of mirror in sample arm. (b) The Doppler shifts of the static tissue background and moving particles.

successfully demonstrated the visualization of the cerebral microcirculation in adult live mice with either skull left intact[19] or skin left intact.[25] In addition, a side product of such treatment is that it enables the full-range complex OCT imaging of biotissues without any additional modification in the conventional OCT system, doubling the ranging distance for FD-OCT.[26–28]

Compared with Doppler OCT that utilizes phase-resolved information,[29] OAG generates flow images with higher contrast since its flow signal appears in the negative depth plane that is free of background noise. The advantage of this processing method over Doppler OCT was also reported by Szkulmowski et al.,[20] where it is found through simulations that at higher signal-to-noise ratio (SNR), Doppler domain processing method has the similar contrast to that of Doppler OCT. However, at lower SNR signals, it delivers substantially better contrast over Doppler OCT. Later Tao et al.[30] proposed to use a modified Hilbert transform algorithm without a need of a modulation frequency. In this work, after Fourier transform of 2-D k-t space data along time t axis, a frequency-shifted Heaviside step function was applied to exclude the unwanted Doppler frequencies in k-ω space, which leaves only relative large positive ω. This operation is equivalent to shifting all the Doppler frequencies by a modulation frequency with only relative large magnitude ω left as negative values, as proposed in Ref. 19. Then Fourier transform is applied along the k axis to generate the volumetric flow network as demonstrated by imaging a live chicken embryo.[30]

The Doppler domain processing method entails dense A-scans in one B scan to ensure enough sampling points to acquire the Doppler shifts. From Eq. (4), the maximum detectable velocity is

$$v_{\max} = \frac{\pi}{2k_0 t}. \tag{7}$$

Thus, an increase of A-scan rate, hence a reduction of the time interval t, leads to an increase of velocity detection range.

Alternatively, as indicated from Eq. (1), the Fourier transform of the raw spectrum in k-space leads to OCT signals in complex number, which can be directly analyzed to image the blood flow. Although not in the domain of OCT-based angiography, Wang et al. reported, in 2004, the first utilization of the complex number including both phase and magnitude information in FD-OCT for flow identification by calculating the so-called Doppler variance σ^2,[31] which was defined as

$$\sigma^2 = \frac{1}{T^2}\left\{1 - \frac{\left|\frac{1}{N}\sum_{j=1}^{N}[f_j(z)\cdot f_{j+1}^*(z)]\right|}{\frac{1}{N}\sum_{j=1}^{N}[f_j(z)\cdot f_j^*(z)]}\right\}, \tag{8}$$

where T is the time interval between adjacent A-scans; N is number of A-line scans employed for averaging; j is the index of A-line scan within N; $f_j(z)$ is the complex OCT results after Fourier transform of the k space spectrum; $f_j^*(z)$ is the complex conjugate of $f_j(z)$. The scanning protocol belongs to Doppler domain processing method, where the dense A-line scans are performed within one B-scan and the Doppler variance is evaluated between neighboring A-line scans. Here, the Doppler variance is similar to the concept of phase variance. The flow contrast comes from the summation of complex number multiplications $\sum_{j=1}^{N}[f_j(z)\cdot f_{j+1}^*(z)]$, where $f_j(z)$ tends to lead to smaller results. In essence, it estimates the variance of $f_j(z)$ within N averaging window, which depends on the flow velocity distribution. Thus, the variations of flow velocity would lead to a larger Doppler variance. Later, Yu and Chen[32] extended this work to perform angiography of the retina and choroid by the use of Doppler variance with histogram-based bulk motion compensation.[32] In this work, one three-dimensional (3-D) scan contains 128 B-scans each of which consist of 2048 dense A-line scans covering 2.5 mm × 2.5 mm area. One key feature of the Doppler variance is that Doppler OCT can also be readily performed since Doppler variance and Doppler OCT share the same scanning protocol while Doppler variance provides more detailed vasculature than Doppler OCT.[32] Later, Liu et al.,[33] reported an intensity-based Doppler variance algorithm in which Eq. (8) is modified as

$$\sigma^2 = \frac{1}{T^2}\left\{1 - \frac{\frac{1}{N}\sum_{j=1}^{N}|f_j(z)\cdot f_{j+1}^*(z)|}{\frac{1}{N}\sum_{j=1}^{N}[f_j(z)\cdot f_j^*(z)]}\right\}. \tag{9}$$

From Eq. (9), the calculation of Doppler variance is no longer dependent on the phase of $f_j(z)$, as demonstrated in Ref. 33, which generates cleaner picture than Doppler variance and Doppler OCT when the phase of the system is not stable due to, for example, time jitter in the SS-OCT system.

2.2 *Ultrahigh-Sensitive Optical Microangiography Based on Complex Optical Coherence Tomography Signal*

The above-mentioned Doppler domain processing method explores the changes in signal frequency exerted on the phases of OCT signal in the k-ω space after taking Fourier transform of the B-scan data along scanning axis (note that this is not in the depth direction). Mathematically, such approach assumes that the changes in the magnitude of Eq. (1) are not considered in the formulation of the problem. For this to be valid, the tissue reflectivity at depth is required to be constant over the time during probe scanning. This condition would be fulfilled only when

the flow and tissue are optically homogeneous. However, in practice, the tissue and blood flow are optically heterogeneous, leading to a fluctuation in the reflectivity of tissue, i.e., $r_S(z_j)$ is a function of scanning time. Indeed, this is the cause of frequency broadening of the background tissue, as shown in Fig. 1(b). Therefore, the overlapping of broadened background frequency components due to heterogeneous optical properties and small Doppler effect due to slow moving particles reduces the detection sensitivity to small functional vessels, for example, capillary flows, within tissue beds.

The recent development of OAG comes with much simpler implementation by utilizing a direct subtraction of neighboring B frames acquired in B-M mode known as ultrahigh-sensitive OMAG.[34,35] In OMAG, instead of operating on phase or intensity alone, the subtraction is performed directly upon the raw spectrum in k-space followed by Fourier transform to generate the flow image. The OCT data $I_{\mathrm{OCT}}(x,z)$ to generate the angiographic results before Fourier transform is

$$S_{\mathrm{OMAG}}(x,k) = S_{i+1}(x,k) - S_i(x,k), \tag{10}$$

where $S_i(x,k)$ is the i'th 2-D k-x space raw data in the slow axis; x is the lateral position in the fast scan direction; k is the k space component. This operation is equivalent to first taking the Fourier transform of the 2-D k-x space data and then performing the subtraction considering the fact that the Fourier transform is a linear operation.

$$I_{\mathrm{OMAG}}(x,z) = I_{i+1}(x,z) - I_i(x,z), \tag{11}$$

where Eqs. (10) and (11) are a Fourier transform pair. Therefore, OMAG is regarded as a method based on complex function of OCT signals, and final result is obtained by taking magnitude of Eq. (11). Compared with Ref. 19, the subtraction operation can be approximated as high-pass filtering the data along the slow axis, which is similar to original OAG that performs the filtering along fast axis. Though conceptually similar, OMAG boasts much better sensitivity owing to the increased time interval between two consecutive measurements using repeated B-scans.

The advantages of OMAG over the algorithms utilizing either phase or intensity are as follows. Considering a general case of blood vessel detection, as illustrated in Fig. 2(a), the moving red blood cells induce both phase and intensity changes in the detected OCT signals. The phase information is obtained by measuring the phase change between adjacent scans, which strongly depends on the incident angle and is sometimes further subject to the phase wrapping problem. Thus, for the case, as indicated in Fig. 2(b), where the majority of blood vessels are nearly perpendicular to the OCT sample beam, for example, in retinal microcirculation, the algorithm based solely on phase information tends to have lower sensitivity. The intensity information is based on the correlation or difference of the pixel values evaluated among repeated measurements, which on the other hand, has difficulty in slow flow detection if the flow only induces the change in phase instead of the change in intensity. The OMAG employs the subtraction of complex numbers, overcoming these problems by operating in complex domain. Hence, it would be expected to result in better results than the methods relying solely on phase or intensity.

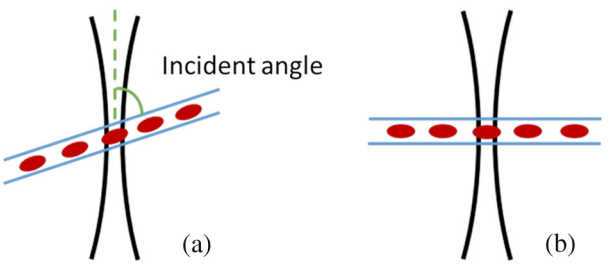

Fig. 2 Configurations of incident sample beam and blood vessel: (a) general case; (b) case where blood vessel is perpendicular to the sample beam.

In Ref. 34, the authors demonstrated the concept by the use of a SD-OCT system operating at 47-kHz A-scan rate. Each volumetric dataset consists of 1500 B-scans with 128 A-line scans in each B scan covering 2 mm × 2 mm area. The performance of OMAG was demonstrated through *in vivo* human skin imaging. Compared with OAG, OMAG has much higher sensitivity, leading to an ability to visualize more vascular details. The microcirculation networks at the different depths of skin were visualized in this work. In parallel, Wang et al.[35] presented the capillary networks in retina and choroid using OMAG. One 3-D scan of 3 mm × 3 mm was acquired within 3 s. The detailed capillary networks at different depths of the posterior eye were visualized. A similar algorithm was also proposed by Srinivasan et al.,[36] in which the angiogram was obtained by taking the difference of the weighted complex numbers acquired between adjacent B-scans. In this work, the cortical microvasculature in rat model was visualized *in vivo* and the reorganization of capillary flow was observed.

Yousefi et al.[37] presented an important alternative technique based on multiple signal classification approach to separate the signals that are caused by particle motion from the signals due to the static tissue components. Similar to OMAG, this approach is a filtering technique that was developed upon eigen-decomposition of the received OCT signals,[38] based on the principle of orthogonality. The property of orthogonality gives that the noise subspace eigenvectors of the autocorrelation matrix (or the data matrix) are orthogonal to the signal eigenvectors, or any linear combination of the signal eigenvectors.[39] Based on this property, OCT signal at each spatial location can be modeled as the superposition of tissue signal (stationary and nonmoving structure information), motion signal (mostly influenced by moving red blood cells), and noise (shot noise and system noise). There are two important assumptions in this approach: (1) static tissue signal, motion signal, and noise are independent to each other and can be decomposed into orthogonal basis functions and (2) the static tissue signal is the most dominant portion of the received OCT signal. The latter assumption is, however, a drawback because when there is very strong flow signal present in the OCT signal, the order of the eigenvalues would change and the largest eigenvalue is no longer corresponding to the static tissue signals. Nevertheless, the authors have used this multiple signal classification approach to successfully achieve the mapping of functional microvascular networks within skin tissue *in vivo*.

2.3 *Angiography Based on the Intensity of Optical Coherence Tomography Signal*

The second category of the OCT angiography is based on the intensity of the OCT signal, sometimes referring to the magnitude of the right-hand side of Eq. (2). A key advantage of the intensity-based OCT angiography is that it is relatively less sensitive to phase noise, making it particularly helpful in situations where the phase stability of light source is an issue.[40] On the

other hand, however, the removal of phase information in the formulation of the problem may sometimes cause difficulty in cases where the flow induces the change only in the phase of OCT signal, rather than in the reflectivity of the moving particles.

We may describe the intensity or speckle of the OCT signal as the random interference pattern produced by the coherent backscattered light from a random medium. The speckle pattern is associated with the movement of scattering particles in random medium since such movement would cause phase shift in the backscattered light that consequently would lead to a change in random interference pattern.[41,42] Hence, the temporal and spatial statistics of the speckle pattern contain the information of the motion of the scattering particles. If an OCT image is acquired from a stationary object, the speckle pattern is temporally stationary; in contrast, if an OCT image is acquired from an object of moving particles, for example, intralipid solution, the speckle pattern would vary with time. By analyzing the temporal or spatial statistics of the intensity or speckle from OCT images, blood vessels can be identified. Such contrast mechanism has also a weak dependence, if not totally independent, on the Doppler angle in contrast to Doppler OCT.[43]

The first work to our knowledge utilizing the speckle concept for flow detection was proposed by Barton and Stromski[44] in 2005 by the use of time-domain OCT system. In this work, the time-varying speckle was manifested as a change in spatial speckle frequencies in OCT image, which was demonstrated to bear information about flow velocity. With the development of FD-OCT, Mariampillai et al.[43] used this speckle concept to develop a method called speckle variance OCT, by evaluating the speckle variance in the OCT structure intensity across the desired number of B-scan images, preferably acquired at the same location, using the following equation:

$$I_{\mathrm{SV}} = \frac{1}{N}\sum_{i=1}^{N}\left(I_{ijk} - \frac{1}{N}\sum_{i=1}^{N} I_{ijk}\right)^2, \tag{12}$$

where N is the number of B scans, j and k are the lateral and depth indices of the B frame images, respectively, and i denotes the B frame slice index within N. Later, in 2010, Mariampillai et al.[45] further evaluated the optimized conditions for speckle variance OCT imaging of microvasculature. They demonstrated through *in vivo* imaging of the dorsal window chamber model (bulk motion being relatively low) and the nonstabilized human finger (bulk motion being relatively high) that in order to achieve a significant level of image contrast, frame rates must be optimized such that tissue displacement between frames is less than the probe beam radius. Hence, in the case of low tissue motion, a high-sensitive endogenous-contrast microvascular imaging prefers to have large number of B scans while in situations where tissue motion is high, the frame rate during acquisition must be optimized to keep interframe displacements to be less than the beam waist radius. In this work, the image was acquired using a 36-kHz A-scan rate Fourier-domain mode locking (FDML) SS with 800 A-scans in each B-scan covering a 5-mm range. The B-scan repetition number N was selected to be 2, 4, 8, 16, and 32 for a comparison study. Recently Xu et al.[46] demonstrated real-time human retinal angiography using speckle variance OCT. Comparing with FA, the density of capillary microvasculature acquired using speckle variance OCT was visibly greater. It was indicated in this work that speckle variance OCT was able to detect microvasculature via intrinsic scattering contrast of red blood cells as they move through the vascular networks in human retina.

Similar to the evaluation of the speckle variance of OCT images, Blatter et al.[47] used an FDML SS operating at an A-scan rate of up to 1.68 MHz to calculate the squared intensity difference in logarithm between successive B-scans for microcirculation imaging:

$$I_{\mathrm{Flow}} = [I(x, y_i, z) - I(x, y_{i+1}, z)]^2, \tag{13}$$

where $I(x, y, z) = 20\ \log[|\mathrm{FFT}(x, y, k)|]$ and x, y, z are the spatial pixel coordinates corresponding to fast and slow scanning axis and the depth coordinate, respectively. In this work, the image was obtained with five B-scan repetitions at the same lateral position, each of which consists of 2060 A-scans. Owning to the fast speed of the SS-OCT system, the retinal microvasculature was acquired within a few seconds over ~48 deg in a single recording without the need of postimage stitching.

On the other hand, Huang et al.[48] later proposed an even simpler scheme to achieve angiography of the retinal vasculature by directly performing subtraction of the OCT intensity between adjacent B-scans as:

$$I_{\mathrm{Flow}} = \frac{1}{N-1}\sum_{i=0}^{N-1} |I_{i+1}(x, z) - I_i(x, z)|, \tag{14}$$

where N is the number of B-scan repetition, x and z are the spatial pixel coordinates in the fast scan direction and depth, respectively. In contrast to Ref. 47, $I_i(x, z)$ refers to the linear magnitude instead of the magnitude in logarithm. The authors in this work used a Cirrus prototype with an SS laser provided by Carl Zeiss Meditec (Dublin, California) to demonstrate the clinical utility of the algorithm. Four B-scans were repeated in each lateral position with 300 A-scans in each B-scan covering ~3 mm on the retinal surface. This method has been shown to provide an ability to detect and monitor the abnormal microvasculature in macular telangiectasia type 2 (Mac-Tel2) eyes.[49]

Without the use of the motion-contrast concept, Yasuno et al.[50] instead proposed a direct intensity-threshold-based angiography, based on the fact that the blood vessels in choroid are often visualized as regions of low signal in the structural OCT images.[50] Hence, this simple but effective method is more suited for choroid vasculature imaging.

Alternatively, Jonathan et al.[51] proposed a so-called correlation mapping method that was further investigated by Enfield et al.[52] Correlation mapping allows for the differentiation of flow regions since static regions usually have high correlation values while flow regions have lower correlation values.[53] The correlation mapping parameter between two consecutive frames is calculated as[54]

$$I_{\mathrm{cm}}(x, y) = \frac{\sum_{p=1}^{M}\sum_{q=1}^{N}\{[I_A(x+p, y+q) - \overline{I_A(x, y)}][I_B(x+p, y+q) - \overline{I_B(x, y)}]\}}{\sqrt{\sum_{p=1}^{M}\sum_{q=1}^{N}[I_A(x+p, y+q) - \overline{I_A(x, y)}]^2}\sqrt{\sum_{p=1}^{M}\sum_{q=1}^{N}[I_B(x+p, y+q) - \overline{I_B(x, y)}]^2}}, \tag{15}$$

where $M \times N$ defines the window size for averaging; IA and IB are a pair of neighboring subimages; $\overline{I_A}$ and $\overline{I_B}$ denote the mean values of IA and IB, respectively. It is worth mentioning that region where the intensity signal is of low contrast, such as the background, would have weak correlation. Hence, a binary mask based on the structural information has to be applied onto the correlation mapping results to eliminate the low structural intensity regions in final microvascular map. In Ref. 54, this mask was generated by performing a blurring kernel followed by a binary threshold on the structural OCT image.

In addition to the aforementioned intensity-based OCT angiography, Jia et al.[55,56] proposed a split-spectrum amplitude-decorrelation angiography (SSADA), in which the decorrelation (i.e., the inverse correlation) between two consecutive B-scans from the narrowed spectral bands was computed, and all the decorrelation values within certain repeated B-scans were averaged to visualize blood vessels. The concept of decorrelation to contrast blood flow is the same as that of the correlation mapping approach. The employment of split spectrum has formerly been demonstrated (i.e., frequency compounding approach) for speckle reduction in OCT.[57,58] Based on the fact that the speckle pattern is spectral dependent, frequency compounding approach reduces this spectral-dependent speckle noise in the structural image at the cost of worsened axial resolution. Hereby, such principle is applied to the flow-generated speckle signals. By splitting the full OCT spectrum into several narrower bands, the averaged decorrelation tends to be more (spectral) speckle noise independent. Therefore, it would be expected that the SSADA algorithm should primarily provide an improvement over the existing correlation mapping algorithm through the reduction of spectral speckle noise. It is, however, important to note that the flow generated OCT signal is sensed by all the wavelengths of the light source under either one exposure of the camera employed in spectrometer for SD-OCT configuration or very short acquisition time period (a few microseconds or less) owing to the high sampling speed of digitizers for SS-OCT configurations. Thus, considering the physical condition, for example, the speed of red blood cells, the speckle statistics should remain unaltered among all the split spectra at one exposure, whereas the moving red blood cells would induce time varying speckles, which can often be observed between adjacent A-scans or B-scans.

Nevertheless, the SSADA algorithm has been reported to deliver the ability to contrast blood flow within retina with higher sensitivity than the results not employing split spectrum scheme. In the method proposed by Jia et al.,[55] the k-space raw spectrum was firstly Gaussian filtered into M bands, each of which was then Fourier transformed to generate intensity images. Decorrelation was evaluated based on all these intensity images as

$$D(x,z) = 1 - \frac{1}{N-1}\frac{1}{M}\sum_{n=1}^{N-1}\sum_{m=1}^{M}\frac{A_n(x,z)A_{n+1}(x,z)}{\left[\frac{1}{2}A_n(x,z)^2 + \frac{1}{2}A_{n+1}(x,z)^2\right]}, \tag{16}$$

where M is the number of split spectra, N is the repetition of B-scans. It is no surprise from Eq. (16) and correlation theory that the flow would lead to high decorrelation while the static background would generate low decorrelation. However, due to the nature of decorrelation, the tissue region where the signal intensity is low (hence, OCT signals appear random) would also generate high decorrelation. As such, a binary mask is often applied onto the decorrelation map to remove the artifacts from the lower intensity regions. In Ref. 55, the threshold for the mask was set to 2 standard deviations above the mean background value when the sample beam was blocked. The authors in this work demonstrated this method through the *in vivo* imaging of the human macula and optic nerve head. They showed that SSADA had improved SNR compared to the decorrelation method evaluated using the full spectrum or pixel averaging.

2.4 *Angiography Based on the Phase of Optical Coherence Tomography Signal*

The first demonstration of OCT blood flow imaging based on phase information dated back to Doppler OCT using the time-domain OCT in 1997, in which the flow monitoring was based on the fact that the Doppler shift in backscattered light induced by moving objects is additive to the carrier frequency associated with the reference arm.[29,59] Doppler broadening due to moving particle is observed, which has been utilized to measure the transverse blood flow velocity.[60] Short-time Fourier-transform algorithm was applied upon the time-dependent detector signals to obtain the improved estimation of the localized Doppler spectra from which the mean velocity of the scatters can be evaluated. With the advent of FD-OCT, the first Doppler OCT was reported by Leitgeb et al.[61] and White et al.,[62] respectively, in 2003. The blood flow information was acquired by evaluating the changes in phase between adjacent A-line scans since the phase information, as indicated in Eq. (1), is readily available in FD-OCT. The velocity of the scatters can be calculated from

$$v(z) = \frac{\Delta\Phi(z,\tau)\lambda}{4\pi\tau n}, \tag{17}$$

where $\Delta\Phi(z,\tau)$ and τ are the phase difference and the time interval between two A-line scans; λ is the central wavelength of the light source; n is the refractive index of the tissue. It is noticed that the above efforts were focused on the measurement of blood flow velocity by using the Doppler effect imparted by moving particles. 3-D angiographic imaging, however, is subject to substantial motion of the sample, for example, human eye movement during the scan, especially when acquisition times of several seconds are often required for volumetric imaging.

Due to this fact, the first *in vivo* noninvasive OCT angiography, to the best of our knowledge, was not reported until 2006 by Makita et al.[63] for retinal imaging. The authors in this work reported two mechanisms that were employed to overcome the sample movement in axial direction: (1) compensation of the axial shift between adjacent A-line scans within one B-scan frame using histogram based bulk motion Doppler shift compensation; (2) compensation of the motion between neighboring B-scan frames using the cross-correlation of particular A-lines. After motion compensation, the angiography was obtained as the average of Doppler OCT and power Doppler that was defined as the power of the phase difference between adjacent A-line scans [$\Delta^2\Phi(z,\tau)$]. In this work, the image was acquired at A-scan rate of 18.7 kHz with 1024 A-lines within one B-scan. The histogram-based bulk motion compensation was based on the assumption that the motion-induced phase difference would be at maximum count in the histogram of the phase differences between two adjacent A-line scans. In other words, at least half

of the pixels above noise level within one A-line are not flow, which is generally valid. This useful histogram-based bulk motion compensation has been widely adopted in the most recent OCT angiographic approaches, where the phase information of the OCT signal is utilized.

Later, a dual-beam scanning strategy was proposed in Doppler OCT to improve its sensitivity to measure the blood flow.[64,65] In a brief detail, two individual sample arm beams from two sets of SD-OCT systems are combined such that there is a small horizontal offset between each beam at the sample surface. The Doppler OCT is performed based on these two data sets. The use of two individual SD-OCT systems relaxes the constraint of the requirement of dense A-line scans while providing flexibility to select the time separation between the two sample beams, hence the velocity measurement range. However, two identical SD-OCT systems are required for this concept, which increases system cost and complexity.

Doppler OCT utilizes the phase resolved information to provide the velocity of flow. By doing so, the requirement of dense A-scans would normally be reinforced such that the compared points in adjacent A-lines must be sufficiently close so that the speckle is reasonably correlated for each pixel,[61,62] or simply put, the magnitude in Eq. (1) being relatively constant. This fact limits the time interval for the phase difference calculation between two measurements, making it difficult to image the small functional vessels with relatively slow blood flows, for example, the capillary vessels. This is because to visualize the slow blood flows, it would require relatively longer time interval according to Eq. (17). Another critical reason for the difficulty in slow vessel visualization is the scanning protocol of the dense A-line scans.[21] The evaluation of phase change at each depth z between adjacent A-line scans is under the assumption that this change is caused solely by the moving scatterers within sample. However, even though the adjacent A-line scans are sufficiently close, the variation of refractive index between the successive A-lines will inevitably leads to undesirable small phase changes due to the heterogeneous properties of tissue, which would overlap with the small change in phase due to slow flow, leading to a reduction in detection sensitivity to slow flow. Furthermore, Doppler OCT signal depends critically on the beam incident angle, which limits its detectability in many ways, for example, in the imaging of retinal blood vessels, where the orientation of most retinal blood vessels is almost perpendicular to the incident probe beam.[66,67]

In 2007, Fingler et al.[68] proposed the use of phase variance between adjacent B-scans to visualize transverse flow and later proposed the phase variance-based volumetric microvascular imaging of human retina.[69] The phase variance is calculated as[70]

$$I_{PV} = \frac{1}{N-1}\sum_{i=1}^{N-1}\left[\Delta\Phi_i(x,z) - \frac{1}{N-1}\sum_{i=1}^{N-1}\Delta\Phi_i(x,z)\right]^2, \tag{18}$$

where N represents the repetition number of B-scans; x and z denote the lateral position and depth, respectively. By properly choosing the repeated scanning along the B-scan, i.e., B-M scan, the time separation between phase measurements is significantly increased. As a consequence, the sensitivity to slower flows is dramatically increased even though the velocity information of the flow is lost due to phase wrapping. By using phase variance instead of phase-resolved difference, the vasculature was visualized with less dependence on vessel orientation and flow velocity. In Ref. 69, the authors acquired the data with an A-scan line rate of 25 kHz. Each 3-D dataset was composed of 1000 B-scans with each consisting of 125 A-line scans over 1 mm. Later Kim et al.[70] reported a faster system with image acquisition at 125-kHz A-scan rate and larger field of view for human retinal circulation imaging. In this work, the phase variance OCT angiography was also compared with fundus FA images.

Similarly, Vakoc et al.[71] proposed to use amplitude-weighed phase variance to monitor tumor microenvironment *in vivo* in which each phase difference was weighted by the magnitude of the average signal at the pixel before the variances were calculated. The amplitude weighting would minimize the phase decorrelation artifacts due to the background optical heterogeneity and reduce the motion artifacts due to for example respiration and muscular contractions.[71] After complicated post-processing procedures, the authors were able to present images of tumor angiogenesis in mouse brain. Alternatively, Kurokawa et al.[72] proposed the use of Doppler power imaging with adaptive optics in which the image pixel value is determined by the squared power of Doppler shift $[\Delta^2\Phi(z,\tau)]$. While the flow contrast mechanism is the same as those reported previously, the use of adaptive optics would result in an increased lateral resolution for vascular imaging.

2.5 *Potential Future Directions of Technical Development in Optical Coherence Tomography Angiography*

The above sections summarize the different OCT angiographies based on phase, magnitude, or both (i.e., the complex function) of the OCT signals. Each method has its own merits due to its unique physics and mathematics behind the flow contrast mechanism. It would be interesting in future to investigate a case where more than one algorithm is employed in one integrated method, leveraging the advantages offered by each algorithm. Some of the reports in literature have already started to investigate the potential benefits being offered by synergistically integrating different algorithms into one effort to improve the angiographic results.

In 2009, Wang et al. proposed a so-called Doppler OMAG (DOMAG),[22] which combine the OAG/OMAG[19] with Doppler OCT. The traditional Doppler OCT suffers from heterogeneous tissue background that limits the detection of slow flows as mentioned in Sec. 2.3 but provides velocity information of the flows. However, OAG successfully suppresses the tissue background by separating the flow from the static background at negative and positive depth planes, respectively, by using Doppler domain processing, although the flow velocity is lost. The DOMAG takes the advantages of both Doppler OCT and OAG/OMAG. For the implementation reported in Ref. 22, the scanning protocol is exactly the same as Doppler OCT, where each B-scan consists of 1500 A-line scans covering 2.5-mm length. After each B-scan was acquired, the k-t space raw data were transformed to k-ω space using Fourier transform along t direction. In k-ω space, the OCT data were first high-pass filtered to reject low frequency components due to heterogeneous background, which was then synthesized with an artificial DC component mimicking ideal homogeneous tissue background. Inverse Fourier transform was then applied along ω direction followed by traditional Doppler OCT processing procedures to generate DOMAG flow image. It was demonstrated through phantom and *in vivo* mouse brain with

intact skull that DOMAG was able to generate the velocity-resolved angiogram with reduced background noise. Using the same dataset, DOMAG boasts a 15-fold lower phase noise level, leading to a much more detailed vasculature when compared with Doppler OCT alone.

Recently, Choi et al.[73] reported an improved blood vessel network imaging of *in vivo* human skin using OMAG with a correlation mapping mask. The rationale behind this approach is that in OMAG, the residue signals of high intensity static background might be comparable to regions of small blood vessels in the angiograms, while correlation mapping has a weak dependence on the structural intensity due to the normalized calculation. Thus, it would be expected that a combined use of these two approaches would result in a better image contrast in terms of the visualization of functional vascular network within tissue. After the structural data were acquired in B-M mode, the authors in this work first employed the correlation-mapping algorithm to generate a binary mask data based on intensity thresholding, which was then applied to mask the results of OMAG to generate the final angiograms. It was demonstrated through *in vivo* human skin tissue in Ref. 73 that the use of OMAG together with a correlation mapping leads to higher SNR than using OMAG or correlation mapping alone. A similar idea was also proposed by Huang et al.,[74] in which the results of OMAG were weighted by the pixelwise decorrelation coefficient. By the use of this combination, it was demonstrated through clinical data from patients' eyes that the hyperreflective foci in retina can be efficiently removed, indicating its potential clinical values of such approach.

Most recently, Zhang and Wang[75] proposed a novel feature space-based optical microangiography method (fsOMAG) in which the flow and static background were effectively differentiated in the feature space, leading to the essential suppression of angiographic signals from the static background. In brief, after the OMAG results were obtained, each pixel in the angiogram was projected onto a feature space utilizing the structural intensity signals. The x axis of the feature space denotes the ratio between the flow intensity and the structural intensity ($I_{\text{flow}}/I_{\text{structure}}$), and the y axis denotes the logarithm to base 10 of the structural intensity [$\log_{10}(I_{\text{structure}})$]. As demonstrated in Ref. 75, the two groups, namely flow and static background, were well classified on the feature space. The rationale behind this work is that the evaluation of the difference between two repeated measurements as flow contrast is sometimes affected by the structural intensity such that pixels with higher intensity tend to result in higher signal in the angiogram than pixels with lower intensity under otherwise the same condition. By employing the structural intensity as an extra parameter for flow identification, the fsOMAG was demonstrated to have improved performance over OMAG through phantom experiments and *in vivo* human retinal imaging.

In future, we expect to see more algorithms that combine more than one contrast mechanisms to achieve better image contrast of OCT-based angiograms, facilitating the quantification of vascular involvement in diseases.

3 Quantitative Comparisons

Due to the rapid development of OCT-based angiography technique, we realize that it would be hard to evaluate the advantages and disadvantages of various existing algorithms based on currently existing literature. Although different algorithms have been demonstrated with promising results in the literature, it is clearly difficult to compare their relative strengths and weakness due to various factors that may impact results, performance, and image quality. Those factors include, but may not be limited to: (1) the capabilities and specifications of hardware imaging platform that each study employed, e.g., speed, sensitivity, SS-OCT versus SD-OCT (sensitivity rolloff), wavelength, system phase stability, etc; (2) patient selection for the study, e.g., normal and various diseased eyes; (3) besides the flow-contrast algorithm, there may involve various postprocessing steps, such as segmentation, 2-D or 3-D filtering, motion correction, etc., to arrive at the final results; and (4) there may involve some preprocessing steps before the flow-contrast algorithm is used to contrast the blood flow, such as motion correction prior to interframe analysis. So far, there has been no systematic study to be able to objectively compare the merits of different OCT angiographic algorithms without unintended biases that may have been caused by the factors listed above. Hence, it is critical to be able to evaluate the relative performance and results of different OCT angiographic algorithms without being restricted by any of these limitations.

For the reasons stated above, in this section, we attempt to compare the performances delivered by several recently proposed algorithms by using the datasets captured from the same retina of human subjects using the same imaging platform. The same datasets were used for each algorithm to derive the microvascular networks innervating retina. Preprocessing to prepare the dataset before and postprocessing after applying flow-contrasting methods were identical for each algorithm compared. In this way, we would be able to somewhat remove the limitations caused by the above mentioned variables in the evaluation. The algorithms that are evaluated in this section include OMAG,[34] speckle variance,[43] phase variance,[70] SSADA,[55] and correlation mapping.[54] Due to the B-M mode scanning, some algorithms, which require repeated A-line scans in each B-scan, such as Doppler OCT,[64] Doppler variance,[32] and DOMAG,[22] were not included in the comparison.

To have the datasets for comparison, we used a 67-kHz Cirrus 5000 HD-OCT angiography prototype system (central wavelength = 840 nm, and bandwidth = 45 nm) (Carl Zeiss Meditec Inc, Dublin, California) to capture the raw data from the subjects enrolled in our existing clinical study. Briefly, the scanning protocol included an angiography scan pattern that was used to generate a volumetric dataset over a 2.4 mm × 2.4 mm area centered at fovea. Each single B-scan was composed of 245 A-scans. For each A-scan, 1024 sampling points were generated along a 2.0-mm axial scan depth. Four consecutive B-scans were acquired at each fixed transversal location before the scanning probe moving to the next transversal location on the retina surface. A total of 245 transversal locations, locating ~9.8-μm apart, were sampled. The time difference between two successive B-scans was roughly 3.7 ms, which corresponds to a B-scan acquisition rate of 270 B-scans per second. One normal subject and one subject diagnosed with DR were included in this comparative study. The Institutional Review Board of University of Washington and ethics committee approval was obtained for the clinical investigational study, and the informed consent was obtained from all subjects before imaging. This study followed the tenets of the Declaration of Helsinki and was conducted in compliance with the Health Insurance Portability and Accountability Act.

In the evaluation, OMAG was implemented using Eq. (11). From four repeated B-scans, three subtractions were performed

between adjacent B-scans, which were then averaged to give the final angiographic results. Speckle variance and phase variance were implemented using Eqs. (12) and (18), respectively. SSADA algorithm was implemented using Eq. (16), where the number of split spectra was selected as 4. The full-width at half-maximum (FWHM) of each Gaussian bandwidth filter was one quarter of the FWHM of the spectrum received by CCD camera employed in the spectrometer. Correlation mapping algorithm was implemented using Eq. (15), where a 3×3 window size was employed for pixel averaging. Thus, unlike SSADA, which also relies on decorrelation, both lateral and axial resolutions are reduced in correlation mapping algorithm. For all the tested algorithms, the sample motion was compensated based on the cross-correlation of adjacent B-scans within each set of repeated measurements. For OMAG and phase variance methods that involve phase evaluation, the histogram-based phase compensation was employed.[63] For phase variance, SSADA and correlation mapping methods that require an intensity thresholding mask to eliminate the false angiographic signals from the low intensity regions, the same mask was applied to exclude the angiographic results from the areas with intensity less than 10 dB above the noise floor.[69,72]

The angiograms of the retinal blood vessel networks from the normal subject were illustrated in Figs. 3(a)–3(e) using OMAG, speckle variance, phase variance, SSADA, and correlation mapping, respectively. It is clear from Fig. 3 that each algorithm provides an ability to visualize the vascular network within the retina but to a different clarity, i.e., contrast. Among the methods compared, the OMAG and speckle variance arguably give better visual results.

From the physiology and anatomy, it is known that the retina tissue is perfused with well-organized and hierarchical vascular plexus that are served to supply the necessary nutritional substances to the different layers of retina. From this aspect, the retinal layer was segmented into two distinct physiological layers, i.e., inner and outer layers, for further detailed comparison. The inner layer covers a layer from anterior retina (i.e., inner limiting membrane) to inner nuclear layer, while the outer retina is from outer plexus layer to outer nuclear layer. To do segmentation, custom-designed semiautomatic segmentation software[76] was used on the available OCT volumetric dataset, the results of which were applied to all the algorithms in concern to generate the depth-resolved angiograms. Figures 4 and 5 illustrated the inner retinal blood vessel network and outer retinal blood vessel network, provided by these methods. Both Figs. 4(a)–4(e) and 5(a)–5(e) correspond to the results obtained using OMAG, speckle variance, phase variance, SSADA, and correlation mapping, respectively. Visually, OMAG delivers the best results for both the inner and outer retinal layers, in terms of noise and vessel connectivity.

Next, we evaluated the performance of each algorithm in contrasting the retinal microvessels, judged by three metrics: vessel connectivity, image contrast, and SNR. In doing so, it is ideal to have a ground-truth flow map, which is, however, unavailable for *in vivo* studies. To solve this problem, we opted for leveraging the images generated by all the algorithms in concern, with which we produced one image by averaging them together with a treatment of giving equal weight for each individual algorithm. The resulted image was then taken as the "ground truth," from which a vascular mask made of skeletonized vessel network with 1 pixel width (equivalent to $\sim 10\ \mu$m) was generated, using the morphological operation proposed in Ref. 77. Figure 3(f) illustrates the skeletonized vascular network mask $M(x, y)$. The vessel connectivity is defined as the standard deviation of the intensity of angiogram that is exactly coregistered with the mask $M(x, y)$, as indicated in Eq. (19):

$$\text{Connectivity} = \text{std}[I(x, y)|_{M(x,y)==1}], \tag{19}$$

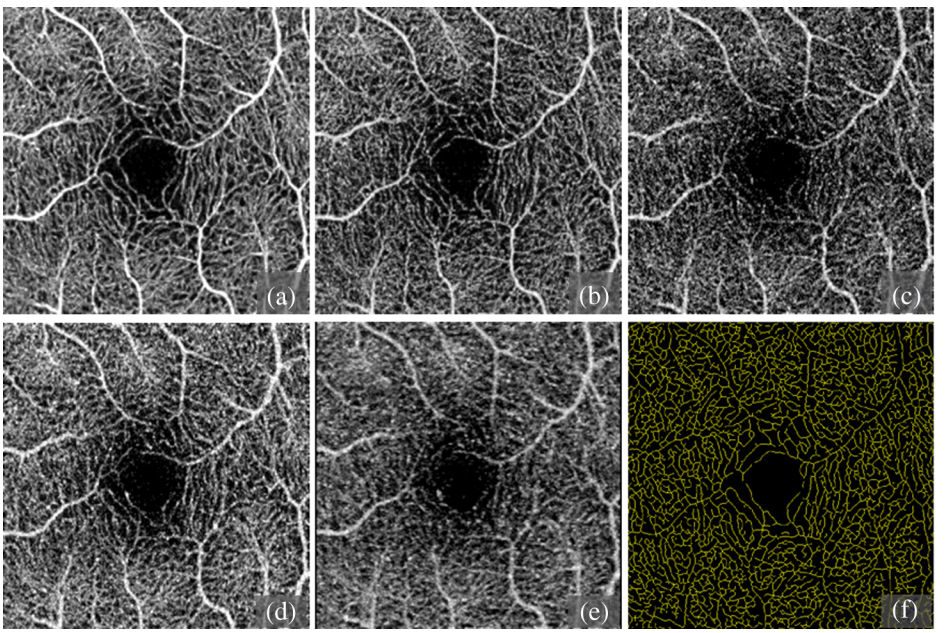

Fig. 3 The performance comparisons. (a)–(e) The blood vessel network in normal human retina visualized by optical microangiography (OMAG), speckle variance, phase variance, split-spectrum amplitude-decorrelation angiography (SSADA), and correlation mapping. (f) The capillaries selected as in yellow to evaluate the connectivity of the angiogram.

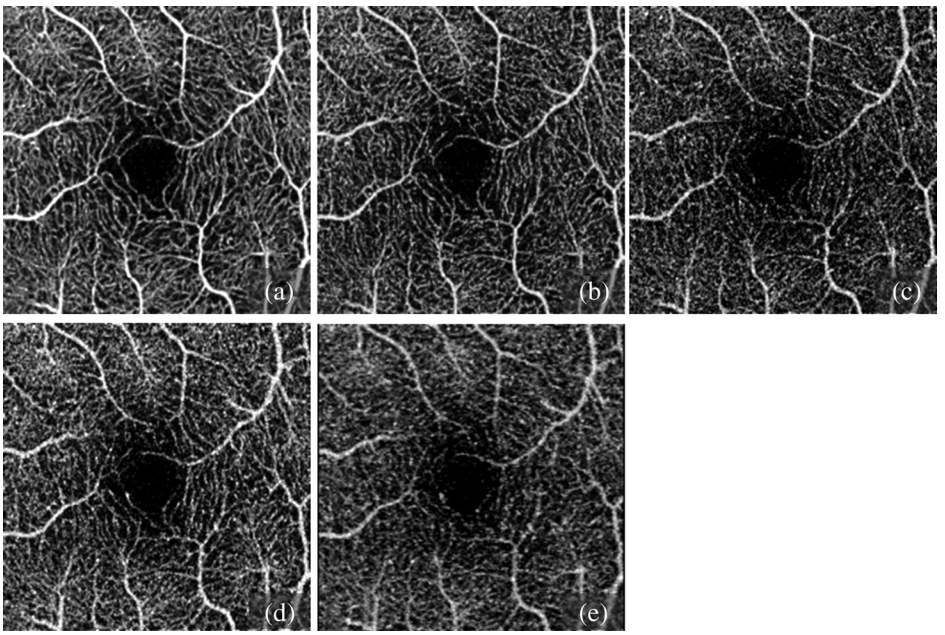

Fig. 4 The performance comparisons. (a)–(e) The blood vessel network in the inner retina layer in normal subject visualized by OMAG, speckle variance, phase variance, SSADA, and correlation mapping.

where $I(x, y)$ denotes the angiogram. The lower this value is, the better mapping performance can an algorithm deliver regarding the connectivity of the angiogram.

The image contrast of the angiograms is defined as

$$\text{Contrast} = \frac{\text{Mean}[I(x,y)|_{M(x,y)==1}]}{\text{Std}[I(x,y)|_{M(x,y)==1}]}, \tag{20}$$

where $\text{Mean}[I(x,y)|_{M(x,y)==1}]$ denotes the mean value of the angiogram intensities on the vascular network mask, as illustrated in Fig. 2(f), and $\text{Std}[I(x,y)|_{M(x,y)==1}]$ denotes the standard deviation of the intensities on the mask.

The SNR of the angiogram is defined by

$$\text{SNR} = \frac{\text{Mean}[I(x,y)|_{M(x,y)==1}]}{\text{Std(background)}}, \tag{21}$$

where $\text{Mean}[I(x,y)|_{M(x,y)==1}]$ denotes the mean value of the intensities on the vascular network mask, and std(background) denotes the standard deviation of background intensity. To define the background area, a thickened vascular network mask was generated based on Fig. 2(f) with pixel width comparable

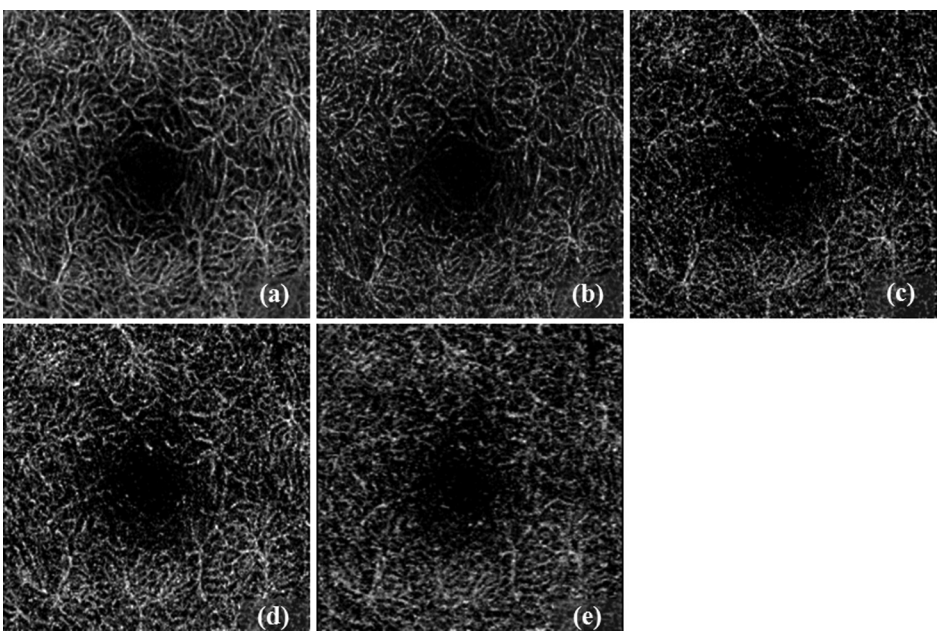

Fig. 5 The performance comparisons. (a)–(e) The blood vessel network in the outer retina layer in normal subject visualized by OMAG, speckle variance, phase variance, SSADA, and correlation mapping.

Table 1 The connectivity, contrast, and signal-to-noise ratio (SNR) comparisons among each algorithm.

	OMAG	Speckle Variance	Phase variance	SSADA	Correlation mapping
Connectivity	0.1693	0.1761	0.1972	0.1934	0.1769
Contrast	3.3602	2.7863	2.2019	2.7276	2.3891
SNR	3.8165	3.3517	2.7282	2.9538	2.5655

Note: OMAG, optical microangiography; SSADA, split-spectrum amplitude-decorrelation angiography.

to the width of large vessels, such that the pixels outside this mask can be considered as background area.

The evaluation of the above three metrics was then performed on the OCT angiograms obtained by each algorithm, as shown in Fig. 3. The results are tabulated in Table 1, where it is indicated that OMAG delivers the best performance overall, at least using the dataset acquired in this study. We suspect that such performance may be delivered by the full use of information content available in OCT signals, i.e., its magnitude and phase information. Comparatively, phase variance approach provides the least performance in terms of vessel connectivity and image contrast while correlation mapping gives the least

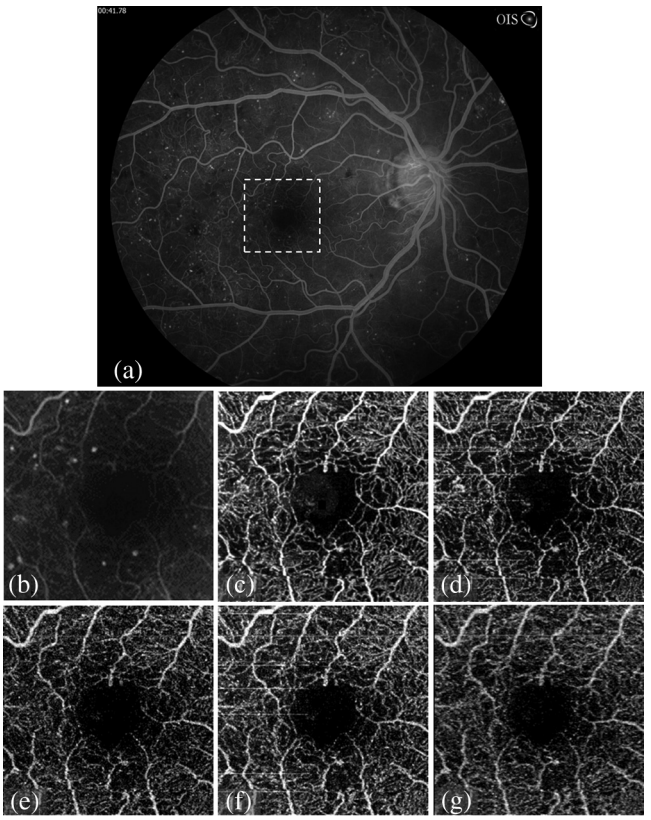

Fig. 6 The performance comparisons using the dataset captured from a subject diagnosed with diabetic retinopathy. (a) Fluorescein angiogram where the scanned area is marked with dashed square box, (b) zoomed fluorescein angiography image corresponding to the area for OCT angiography. (c)–(g) The retinal blood vessel network visualized by OMAG, speckle variance, phase variance, SSADA, and correlation mapping.

Table 2 The computation time from each algorithm.

	OMAG	Speckle variance	Phase variance	SSADA	Correlation mapping
Time (s)	0.0149	0.0150	0.0152	0.231	0.444

performance in terms of SNR. We understand that the comparison study requires a thorough and systematic investigation by the use of properly designed phantoms as well as *in vivo* imaging results. Thus, the results given here may be limited to the dataset used in our study. Future systematic study is therefore warranted.

Next for the pathological case, the data of a subject diagnosed with DR were processed. The DR is a leading cause of blindness in American adults.[78] The fluorescein angiogram of the patient was illustrated in Fig. 6(a). The scanned area for OCT angiography comparisons was denoted by the white dashed box in Fig. 6(a) and zoomed and displayed in Fig. 6(b). Figures 6(c)–6(g) illustrate the angiograms of retinal blood vessel network using OMAG, speckle variance, phase variance, SSADA, and correlation mapping, respectively. Similar to the comparisons in normal subject, OMAG probably leads to the best visual results, which provided a best match with the gold standard fluorescein angiogram, as shown in Fig. 6(b).

The computational cost is another important factor for each algorithm indicating its practicability. Hereby, the time needed to process one lateral position; hence, four repeated B-scans were evaluated for each of the compared algorithms coded with MATLAB processing language run on a laptop with Intel Core i7 processor. The results were listed in Table 2. It is indicated from Table 2 that OMAG, speckle variance method, and phase variance method have small computational cost compared to SSADA and correlation mapping due to the use of simple subtraction operation. For SSADA, the longer time needed is caused by the multiple decorrelation calculations as a result of split spectrum, and for correlation mapping, the pixel averaging leads to the increased time.

4 Conclusion

OCT-based angiography, as one of the most attractive functional extensions to the current popular OCT imaging modality, has been reviewed. The review divided the various OCT-based angiography algorithms into three categories by considering the data type employed for imaging, including the complete (i.e., complex), the intensity and the phase of available OCT signals. The principle of each algorithm has been described with special attention given to the most recently reported and popular ones, including OMAG, speckle variance, phase variance, SSADA, and correlation mapping. A comparative study was performed, which assessed the performances of these methods using the clinical datasets captured from a normal and a pathological retina. From this study, we conclude that among the compared algorithms, complex OCT data based approaches, such as OMAG, may provide the best visual result of retinal microvascular networks in terms of imaging contrast, vessel connectivity, and SNR, most probably owning to the full use of OCT signals. We hope that this review has achieved its purpose to give a general survey on the reported OCT angiography technologies with their blood flow contrast mechanism for those readers, who are interested in the OCT-based angiography.

Acknowledgments

This work was supported in part by the National Institutes of Health with a contract from National Eye Institute (Grant No.: R01-EY024158) and Research to Prevent Blindness (New York, NY). Dr. Wang declares a financial interest in Oregon Health & Science University (OHSU), who owns patents that are relevant to the subject matter discussed in this manuscript. Dr. Wang also receives financial supports from Carl Zeiss Meditec Inc. However, both OHSU and Carl Zeiss Meditec did not support this work.

References

1. D. Huang et al., "Optical coherence tomography," *Science* **254**(5035), 1178–1181 (1991).
2. B. Bouma and G. Tearney, *Handbook of Optical Coherence Tomography*, Taylor & Francis, New York (2001).
3. W. Drexler and J. G. Fujimoto, *Optical Coherence Tomography: Technology and Applications*, Springer Publishing, Berlin, Heidelberg (2008).
4. P. H. Tomolins and R. K. Wang, "Theory, developments and applications of optical coherence tomography," *J. Phys. D: Appl. Phys.* **38**(15), 2519–2535 (2005).
5. W. Drexler et al., "Optical coherence tomography today: speed, contrast, and multimodality," *J. Biomed. Opt.* **19**(7), 071412 (2014).
6. A. M. Zysk et al., "Optical coherence tomography: a review of clinical development from bench to bedside," *J. Biomed. Opt.* **12**(5), 051403 (2007).
7. E. Sattler, R. Kästle, and J. Welzel, "Optical coherence tomography in dermatology," *J. Biomed. Opt.* **18**(6), 061224 (2013).
8. U. Baran et al., "High resolution imaging of acne lesion development and scarring in human facial skin using OCT-based microangiography," *Lasers Surg. Med.* **47**(3), 231–238 (2015).
9. E. Agaynova et al., "Endoscopic OCT with forward-looking probe: clinical studies in urology and gastroenterology," *J. Biophotonics* **1**(2), 114–128 (2008).
10. H. G. Bezerra et al., "Intracoronary optical coherence tomography: a comprehensive review: clinical and research applications," *J. Am. Coll. Cardiol. Intv.* **2**(11), 1035–1046 (2009).
11. S. Dziennis et al., "Macro-to-micro cortical vascular imaging underlies regional differences in ischemic brain," *Sci. Rep.* **5**, 10051 (2015).
12. H.-P. Hammes et al., "Diabetic retinopathy: targeting vasoregression," *Diabetes* **60**(1), 9–16 (2011).
13. J. Flammer et al., "The impact of ocular blood flow in glaucoma," *Prog. Retinal Eye Res.* **21**(4), 359–393 (2002).
14. M. R. Hee et al., "Optical coherence tomography of age-related macular degeneration and choroidal neovascularization," *Ophthalmology* **103**(8), 1260–1270 (1996).
15. J. F. Arevalo, *Retinal Angiography and Optical Coherence Tomography*, Springer, New York (2009).
16. A. F. Fercher et al., "Measurement of intraocular distances by backscattering spectral interferometry," *Opt. Commun.* **117**(1–2), 43–48 (1995).
17. G. Häusler and M. W. Lindner, "Coherence radar and spectral radar–new tools for dermatological diagnosis," *J. Biomed. Opt.* **3**(1), 21–31 (1998).
18. A. Zhang et al., "Generic pixel-wise speckle detection in Fourier-domain optical coherence tomography images," *Opt. Lett.* **39**(15), 4392–4395 (2014).
19. R. K. Wang et al., "Three dimensional optical angiography," *Opt. Express* **15**(7), 4083–4097 (2007).
20. M. Szkulmowski et al., "Flow velocity estimation using joint spectral and time domain optical coherence tomography," *Opt. Express* **16**(9), 6008–6025 (2008).
21. R. K. Wang and Z. Ma, "Real-time flow imaging by removing texture pattern artifacts in spectral-domain optical Doppler tomography," *Opt. Lett.* **31**(20), 3001–3003 (2006).
22. R. K. Wang and L. An, "Doppler optical micro-angiography for volumetric imaging of vascular perfusion in vivo," *Opt. Express* **17**(11), 8926–8940 (2009).
23. R. K. Wang, "Three dimensional optical angiography maps directional blood perfusion deep within microcirculation tissue beds in vivo," *Phys. Med. Biol.* **52**, N531–N537 (2007).
24. R. K. Wang, "Directional blood flow imaging in volumetric optical micro-angiography achieved by digital frequency modulation," *Opt. Lett.* **33**(16), 1878–1880 (2008).
25. R. K. Wang and S. Hurst, "Mapping of cerebrovascular blood perfusion in mice with skin and cranium intact by optical micro-angiography at 1300 nm wavelength," *Opt. Express* **15**(18), 11402–11412 (2007).
26. R. K. Wang, "In vivo full range complex Fourier domain optical coherence tomography," *Appl. Phys. Lett.* **90**, 054103 (2007).
27. L. An and R. K. Wang, "Use of scanner to modulate spatial interferogram for in vivo full range Fourier domain optical coherence tomography," *Opt. Lett.* **32**(23), 3423–3425 (2007).
28. L. An, H. M. Subhash, and R. K. Wang, "Full range complex spectral domain optical coherence tomography for volumetric imaging at 47, 000 A scans per second," *J. Opt.* **12**(8), 084003 (2010).
29. Z. Chen et al., "Noninvasive imaging of in vivo blood flow velocity using optical Doppler tomography," *Opt. Lett.* **22**(14), 1119–1121 (1997).
30. Y. K. Tao, A. M. Davis, and J. A. Izatt, "Single-pass volumetric bidirectional blood flow imaging spectral domain optical coherence tomography using a modified Hilbert transform," *Opt. Express* **16**(16), 12350–12361 (2008).
31. L. Wang et al., "Frequency domain phase-resolved optical Doppler and Doppler variance tomography," *Opt. Commun.* **242**(4–6), 345–350 (2004).
32. L. Yu and Z. Chen, "Doppler variance imaging for three-dimensional retina and choroid angiography," *J. Biomed. Opt.* **15**(1), 016029 (2010).
33. G. Liu et al., "Intensity-based modified Doppler variance algorithm: application to phase instable and phase stable optical coherence tomography systems," *Opt. Express* **19**(12), 11429–11440 (2011).
34. L. An, J. Qin, and R. K. Wang, "Ultrahigh sensitive optical microangiography for in vivo imaging of microcirculations within human skin tissue beds," *Opt. Express* **18**(8), 8220–8228 (2010).
35. R. K. Wang et al., "Depth-resolved imaging of capillary networks in retina and choroid using ultrahigh sensitive optical microangiography," *Opt. Lett.* **35**(9), 1467–1469 (2010).
36. V. J. Srinivasan et al., "Rapid volumetric angiography of cortical microvasculature with optical coherence tomography," *Opt. Lett.* **35**(1), 43–45 (2010).
37. S. Yousefi, J. Qin, and R. K. Wang, "Super-resolution spectral estimation of optical micro-angiography for capillary flow quantification," *Biomed. Opt. Express* **4**(7), 1214–1228 (2013).
38. S. Yousefi, Z. Zhi, and R. K. Wang, "Eigendecomposition-based clutter filtering technique for optical microangiography," *IEEE Trans. Biomed. Eng.* **58**(8), 2316–2323 (2011).
39. S. L. Maple, Jr., *Digital Spectral Analysis with Applications*, Prentice-Hall, New Jersey (1987).
40. H. C. Hendargo et al., "Doppler velocity detection limitations in spectrometer-based versus swept-source optical coherence tomography," *Biomed. Opt. Express* **2**(8), 2175–2188 (2011).
41. J. M. Schmitt, S. H. Xiang, and K. M. Yung, "Speckle in optical coherence tomography," *J. Biomed. Opt.* **4**(1), 95–105 (1999).
42. D. A. Boas and A. K. Dunn, "Laser speckle contrast imaging in biomedical optics," *J. Biomed. Opt.* **15**(1), 011109 (2010).
43. A. Mariampillai et al., "Speckle variance detection of microvasculature using swept-source optical coherence tomography," *Opt. Lett.* **33**(13), 1530–1532 (2008).
44. J. K. Barton and S. Stromski, "Flow measurement without phase information in optical coherence tomography images," *Opt. Express* **13**(14), 5234–5239 (2005).
45. A. Mariampillai et al., "Optimized speckle variance OCT imaging of microvasculature," *Opt. Lett.* **35**(8), 1257–1259 (2010).
46. J. Xu et al., "Retinal angiography with real-time speckle variance optical coherence tomography," *Br. J. Ophthalmol.* **99**(10), 1315–1319 (2015).
47. C. Blatter et al., "Ultrahigh-speed non-invasive widefield angiography," *J. Biomed. Opt.* **17**(7), 070505 (2012).
48. Y. Huang et al., "Swept-source OCT angiography of the retinal vasculature using intensity differentiation-based optical microangiography algorithms," *Ophthalmic Surg. Lasers Imaging Retina* **45**(5), 382–389 (2014).

49. M. R. Thorell et al., "Swept-source OCT angiography of macular telangiectasia type 2," *Ophthalmic Surg. Lasers Imaging Retina* **45**(5), 369–380 (2014).
50. Y. Yasuno et al., "In vivo high-contrast imaging of deep posterior eye by 1-μm swept source optical coherence tomography and scattering optical coherence angiography," *Opt. Express* **15**(10), 6121–6139 (2007).
51. E. Jonathan, J. Enfield, and M. J. Leahy, "Correlation mapping method for generating microcirculation morphology from optical coherence tomography (OCT) intensity images," *J. Biophotonics* **4**(9), 583–587 (2011).
52. J. Enfield, E. Jonathan, and M. J. Leahy, "In vivo imaging of the microcirculation of the volar forearm using correlation mapping optical coherence tomography (cmOCT)," *Biomed. Opt. Express* **2**(5), 1184–1193 (2011).
53. H. M. Subhash and M. J. Leahy, "Microcirculation imaging based on full-range high-speed spectral domain correlation mapping optical coherence tomography," *J. Biomed. Opt.* **19**(2), 021103 (2014).
54. Y. Liew et al., "In vivo assessment of human burn scars through automated quantification of vascularity using optical coherence tomography," *J. Biomed. Opt.* **18**(6), 061213 (2013).
55. Y. Jia et al., "Split-spectrum amplitude-decorrelation angiography with optical coherence tomography," *Opt. Express* **20**(4), 4710–4725 (2012).
56. Y. Jia et al., "Quantitative optical coherence tomography angiography of vascular abnormalities in the living human eye," *Proc. Natl. Acad. Sci. U. S. A.* **112**(18), E2395–E2402 (2015).
57. M. Pircher et al., "Speckle reduction in optical coherence tomography by frequency compounding," *J. Biomed. Opt.* **8**(3), 565–569 (2003).
58. G. van Soest et al., "Frequency domain multiplexing for speckle reduction in optical coherence tomography," *J. Biomed. Opt.* **17**(7), 076018 (2012).
59. J. A. Izatt et al., "In vivo bidirectional color Doppler flow imaging of picoliter blood volumes using optical coherence tomography," *Opt. Lett.* **22**(18), 1439–1441 (1997).
60. S. G. Proskurin, Y. He, and R. K. Wang, "Determination of flow-velocity vector based on doppler shift and spectrum broadening with optical coherence tomography," *Opt. Lett.* **28**(14), 1227–1229 (2003).
61. R. Leitgeb et al., "Real-time assessment of retinal blood flow with ultrafast acquisition by color Doppler Fourier domain optical coherence tomography," *Opt. Express* **11**(23), 3116–3121 (2003).
62. B. White et al., "In vivo dynamic human retinal blood flow imaging using ultra-high-speed spectral domain optical coherence tomography," *Opt. Express* **11**(25), 3490–3497 (2003).
63. S. Makita et al., "Optical coherence angiography," *Opt. Express* **14**(17), 7821–7840 (2006).
64. S. Zotter et al., "Visualization of microvasculature by dual-beam phase-resolved Doppler optical coherence tomography," *Opt. Express* **19**(2), 1217–1227 (2011).
65. S. Makita et al., "Comprehensive in vivo micro-vascular imaging of the human eye by dual-beam-scan Doppler optical coherence angiography," *Opt. Express* **19**(4), 1271–1283 (2011).
66. Y. Wang et al., "Retinal blood flow measurement by circumpapillary Fourier domain Doppler optical coherence tomography," *J. Biomed. Opt.* **13**(6), 064003 (2008).
67. Y. Wang et al., "Retinal blood flow detection in diabetic patients by Doppler Fourier domain optical coherence tomography," *Opt. Express* **17**(5), 4061–4073 (2009).
68. J. Fingler et al., "Mobility and transverse flow visualization using phase variance contrast with spectral domain optical coherence tomography," *Opt. Express* **15**(20), 12636–12653 (2007).
69. J. Fingler et al., "Volumetric microvascular imaging of human retina using optical coherence tomography with a novel motion contrast technique," *Opt. Express* **17**(24), 22190–22200 (2009).
70. D. Yu Kim et al., "In vivo volumetric imaging of human retinal circulation with phase-variance optical coherence tomography," *Biomed. Opt. Express* **2**(6), 1504–1513 (2011).
71. B. J. Vakoc et al., "Three-dimensional microscopy of the tumor microenvironment in vivo using optical frequency domain imaging," *Nat. Med.* **15**(10), 1219–1223 (2009).
72. K. Kurokawa et al., "Three-dimensional retinal and choroidal capillary imaging by power Doppler optical coherence angiography with adaptive optics," *Opt. Express* **20**(20), 22796–22812 (2012)
73. W. Choi et al., "Improved microcirculation imaging of human skin in vivo using optical microangiography with a correlation mapping mask," *J. Biomed. Opt.* **19**(3), 036010 (2014).
74. Y. Huang, Q. Zhang, and R. K. Wang, "Efficient method to suppress artifacts caused by tissue hyper-reflections in optical microangiography of retina in vivo," *Biomed. Opt. Express* **6**(4), 1195–1208 (2015).
75. A. Zhang and R. K. Wang, "Feature space optical coherence tomography based micro-angiography," *Biomed. Opt. Express* **6**(5), 1919–1928 (2015).
76. X. Yin, J. Chao, and R. K. Wang, "User-guided segmentation for volumetric retinal optical coherence tomography images," *J. Biomed. Opt.* **19**(8), 086020 (2014).
77. R. Reif et al., "Quantifying optical microangiography images obtained from a spectral domain optical coherence tomography system," *Int. J. Biomed. Imaging* **2012**, 509783 (2012).
78. J. W. Yau et al., "Global prevalence and major risk factors of diabetic retinopathy," *Diabetes Care* **35**(3), 556–564 (2012).

Biographies for the authors are not available.